Rare Metal Materials and Engineering
Volume 53, Issue 9, September 2024
Available online at www.rmme.ac.cn

Science Press

Cite this article as: Zhang Jingang, Liu Xinling, Chen Xing, et al. Low-Cycle Fatigue Crack Initiation Behavior of Nickel-Based Single Crystal Superalloy[J]. Rare Metal Materials and Engineering, 2024, 53(09): 2458-2467. DOI: 10.12442/j.issn.1002-185X.20230834.

ARTICLE

Low-Cycle Fatigue Crack Initiation Behavior of Nickel-Based Single Crystal Superalloy

Zhang Jingang[1,2], Liu Xinling[1,2], Chen Xing[1,2], Li Zhen[1,2], Li Leyu[1,2], Liu Changkui[1,2]

[1] Failure Analysis Center of Aero Engine Corporation of China, AECC Beijing Institute of Aeronautical Materials, Beijing 100095, China; [2] Beijing Key Laboratory of Aeronautical Materials Testing and Evaluation, Beijing 100095, China

Abstract: Low-cycle fatigue crack initiation behavior of nickel-based single crystal superalloy at 530 °C was investigated. Results show that the behavior of crack initiation is closely related to the maximum strain. When the maximum strain is 2.0%, the fatigue crack is originated at the position of persistent slip bands on the surface of specimen, which is located on the {111} slip plane. No defects are observed at the crack initiation position. When the maximum strain is lower than 1.6%, the cracks are initiated at the casting defects on sub-surface or at interior of the specimen. The casting defects are located on the {100} slip plane vertical to the axial force. The crack is initiated along the {100} slip plane and then expanded along different {111} slip planes after a short stage of expansion. As the maximum strain decreases, the position of crack initiation gradually changes from the surface to the interior. Moreover, the secondary cracks extending inward along the fracture surface appear in the crack initiation area, and there is obvious stress concentration near the secondary cracks. The dislocation density is high near the fracture surface in the crack initiation zone, where a lot of dislocations cutting into the γ' phase exist. An oxide layer of 50–100 nm is presented on the fracture surface, and Ni, Al, Cr and Co elements are mainly segregated into the oxide layer of the surface.

Key words: crack initiation; low-cycle fatigue; single crystal superalloy; casting defects; dislocation density

Nickel-based single crystal (SC) superalloys have been widely used as turbine blade materials in aircraft engines due to their excellent creep resistance and thermal fatigue performance at elevated temperatures[1–3]. In the service process of turbine blades, due to the influence of cyclic thermal stress and alternating load, fatigue failure is prone to occur during the starting and stopping process of engine, which affects the performance of engine. At present, the common failure due to large alternating loads is low-cycle fatigue failure[4–7].

Turbine blades are easily affected by structural factors due to their complex shapes. Therefore, the data of standard fatigue test rod are generally referred to when studying the fatigue performance of SC superalloy. Temperature always plays an important role in the low-cycle fatigue behavior of SC superalloy[8–11]. Previous studies have indicated that the deformation of superalloy at low temperatures is mainly dominated by planar slip[12–14]. Dislocations often move parallel to the {111} slip plane. Liu et al[15] revealed the microscopic deformation mechanism of the cyclic stress response behavior of alloys under different orientations. Li et al[16] found that the specimen eventually shows shear cracks along the slip bands at low temperatures but normal cracks at high temperatures, and shows Mode-I cracking. Zhang et al[17] compared the fatigue behavior of different crystal orientations and found that the crack propagation occurs on the {111} plane after initiation, and then propagation occurs on the planes normal to the tensile stress.

Traditional research mainly focuses on the cyclic hardening and softening behavior of materials during low-cycle fatigue processes[18–19]. In addition, the deformation mechanism of SC superalloys can be investigated by the changes of dislocation morphology[20–22]. Practical studies on the low-cycle fatigue crack initiation behavior of SC superalloys are restricted.

In order to simulate the low-cycle fatigue crack initiation behavior of the tenon part of the real turbine blade, the actual

Received date: December 28, 2023
Foundation item: National Science and Technology Major Project (J2019-VI-0022-0138)
Corresponding author: Liu Xinling, Ph. D., Professor, Failure Analysis Center of Aero Engine Corporation of China, AECC Beijing Institute of Aeronautical Materials, Beijing 100095, P. R. China, E-mail: liuxinling119@163.com

temperature field and load of the blade tenon were analyzed. The test temperature of 530 °C and the strain ratio of 0.05 were chosen as test conditions. By investigating the characteristics of fatigue crack initiation under different loads, the mechanism of low-cycle fatigue crack initiation in SC superalloy was studied. The results of this study will provide support for the service damage behavior of turbine blades in practical engineering.

1 Experiment

The second-generation of nickel-based SC superalloys was used in this work. SC test bar with its length direction parallel to the [001] direction was prepared by spiral crystal selection method in a directional solidification vacuum furnace (ZDG-2). Meanwhile, SC test bar with a deviation less than 15° to the main axis direction was selected as the raw material for the test. The nominal composition of the SC superalloy is listed in Table 1.

Heat treatments of 1290 °C/1 h+1300 °C/2 h+ 1315 °C/4 h (air cooling, AC) +1120 °C/4 h (AC) + 870 °C/32 h (AC) were carried out on the SC test bar. After heat treatment, the γ' phase with typical cubic morphology was uniformly dispersed in the matrix. Macromorphology of SC test bar and microstructure of the matrix are illustrated in Fig. 1a and 1b, respectively. To obtain the low-cycle fatigue performance of the specimen, the fatigue tests were all conducted with the MTS Landmark 370 servo hydraulic testing machine at the temperature of 530 °C. Generally, strain control was adopted during low-cycle fatigue testing. The waveform of fatigue loading was triangular, with a loading rate of 5×10^{-3} s^{-1}. In the fatigue test, maximum strain control was adopted, and the strain ratio was R=0.05. The strain range was controlled by measuring distance with an extensometer.

After the fatigue test, the surface morphology of the fracture was observed by Gemini SEM300 field emission scanning electron microscope (SEM). After low-cycle fatigue tests, longitudinal-section specimens were prepared by wire electrical discharge machining. The longitudinal section of the fracture was mechanically polished to mirror-like state without cracks, followed by vibration polishing for 8 h to remove surface stress. The deformation characteristics near the fracture were obtained by electron back scatter diffraction (EBSD) technique. FEI Scios2 focused ion beam (FIB) was utilized to take microscopic longitudinal section (5 μm×5 μm) on the surface of the fracture, and then it is observed by the transmission electron microscope (TEM). The selected area electron diffraction (SAED) patterns and energy dispersive spectroscope (EDS) spectra were obtained by Talos f200s TEM.

2 Results and Discussion

2.1 Parameter analysis of low-cycle fatigue test

In strain-controlled low-cycle fatigue tests, the relationship between strain and the fatigue cycles is generally analyzed. Meanwhile, the role of other test parameters in fatigue testing is always ignored. The results and process parameters of low-cycle fatigue test are recorded in Table 2. According to the data in Table 2, each test parameter has a certain relationship with the fatigue cycles. The specimen with the maximum strain of 2.0% was named 200-1, and the naming rules for other specimens were similar.

Maximum strain control was adopted in low-cycle fatigue testing in this study, with the strain ratio of R=0.05. The range of maximum strain is 0.75% – 2.0%. Fig. 2a shows the relationship between the maximum strain and cyclic number. The fitted curve shows that the fatigue cycles increase with the decrease in the maximum strain value. At the same time, under the same test conditions, the fatigue cycle life of the

Table1 Elemental composition of nickel-based SC superalloy (wt%)

Cr	Co	W	Mo	Al	Ta	Re	Hf	Nb	Ti	Ni
4.8	9.5	9.0	2.5	6.2	8.5	2.4	0.15	1.2	0.1	Bal.

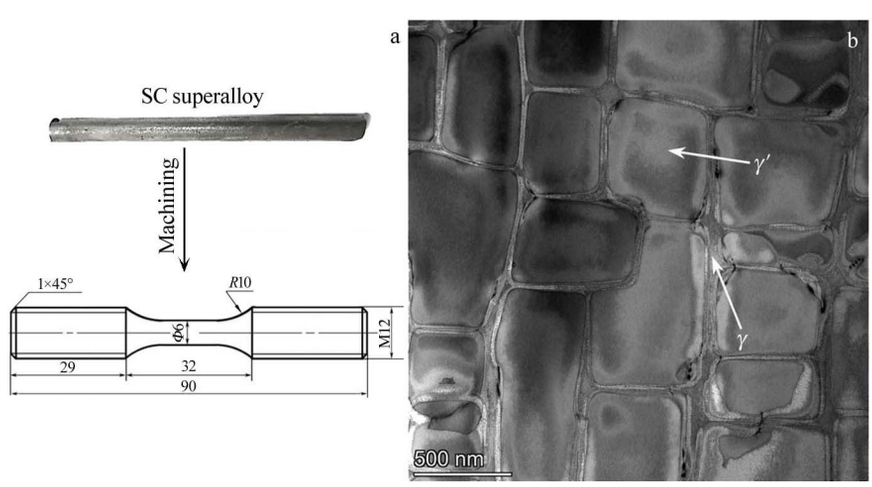

Fig.1 Processing diagram of SC test bar (a) and microstructure of the matrix (b)

Table 2 Fatigue conditions and performance of the specimens

Specimen	f/Hz	σ_{max}/MPa	σ_{min}/MPa	ε_{max}/%	ε_{min}/%	N_f/cycle
200-1	0.132	997	–982	2.000	0.103	61
180-1	0.146	971	–955	1.800	0.091	558
160-1	0.164	980	–729	1.600	0.080	1 542
140-1	0.188	965	–510	1.400	0.070	3 563
120-1	0.219	900	–412	1.200	0.060	28 525
090-1	0.292	898	–53	0.900	0.045	34 294
075-1	0.351	892	–38	0.750	0.037	42 481

specimens exhibits a large dispersion, which is related to the characteristics of SC superalloys. Since the influence of grain boundaries is eliminated during the directional solidification process, anisotropic features are represented in the SC superalloys.

Fig. 2b shows the relationship between test load and the fatigue cycles during the the low-cycle fatigue test. With the increase in fatigue life, the maximum stress shows a decreasing trend. In addition, the minimum stress gradually increases with the increase in fatigue life. According to the value of test monitoring, the maximum stress of the test is always positive, and the load applied to the specimen at the peak of the stress is tensile stress. The minimum stress increases from –982 MPa to 38 MPa, and the applied load at the valley value of the stress is compressive stress. In addition, the compressive stress changes in a large range with the increase in fatigue life compared with tensile stress. During the low-cycle fatigue test with a strain ratio of 0.05, the specimen of SC superalloys is subjected to tensile-compressive fatigue loads.

Fig. 2c shows the relationship between actual stress ratio and the number of cycles during low-cycle fatigue testing. The actual stress ratio is obtained by the ratio of the minimum stress to the maximum stress ($\sigma_{min}/\sigma_{max}$) in the monitoring data. As shown in Fig.2c, the variation process of actual stress ratio can be divided into two stages: stage I and stage II. Taking the fatigue life of 1×10^3 cycles as the boundary, at stage I with a fatigue life less than 1×10^3 cycles, the actual stress ratio of specimens is around – 1. Moreover, when the fatigue life exceeds 1×10^3 cycles at stage II, the actual stress ratio of the specimen gradually increases with the increase in fatigue life. The effect of compression load on fatigue fracture morphology is gradually weakened at stage II.

Fig.2d shows the relationship between the testing frequency of low-cycle fatigue and the number of cycles. With the increase in fatigue life, the testing frequency shows an

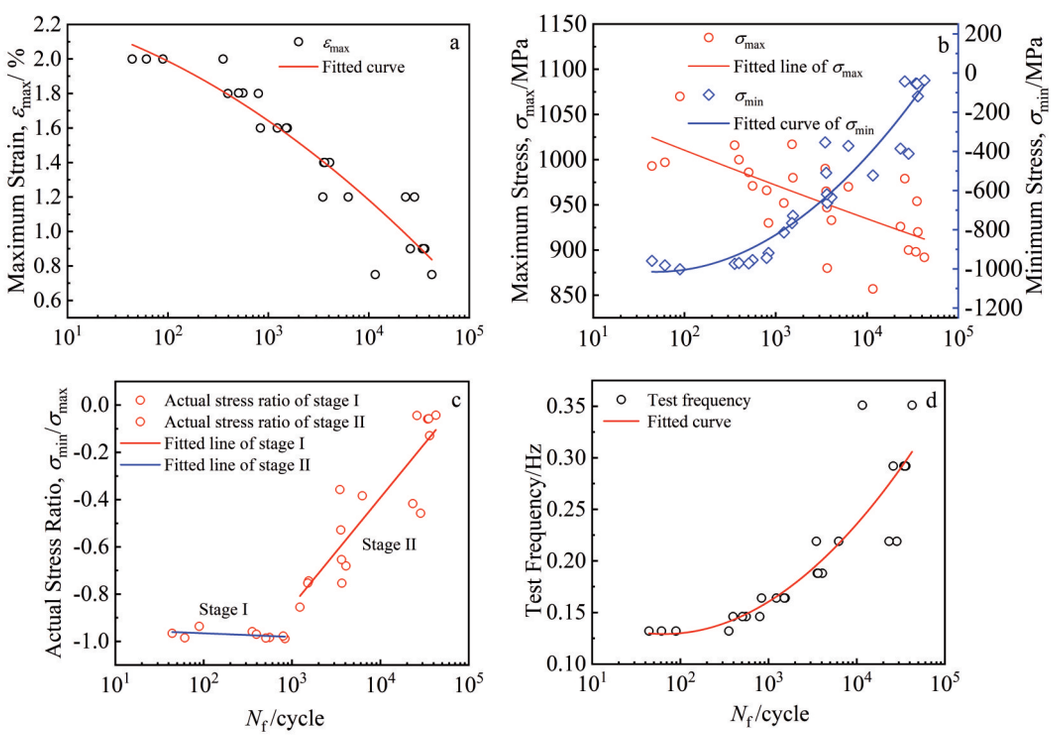

Fig.2 Low-cycle fatigue testing results of nickel-based SC superalloys: (a) maximum strain-cycle life; (b) stress-cycle life; (c) actual stress ratio-cycle life; (d) test frequency-cycle life

increasing trend. According to the fitted curve, the quadratic function relationship is found between the testing frequency and the fatigue life.

2.2 Fracture characteristics during crack initiation stage

Generally, crack propagation of fatigue fracture can be divided into three stages: crack initiation stage, crack propagation stage, and final fracture stage. For low-cycle fatigue fracture of SC superalloys, fatigue life is relatively short during the stage of crack propagation. At the stage of crack initiation, fatigue life accounts for the majority.

Fig.3 shows the macroscopic features of the fracture surface and the microscopic morphology near the crack initiation area. The maximum strain of fracture is 2.0%. Fig. 3a displays two main slip planes of the fracture surface. The extended edges of the fatigue fracture converge near the surface of SC superalloys. Consequently, the crack originates from the surface of the specimen, with a flat fracture in stable propagation stage and a rough sliding step feature in the final rupture region. Due to the typical face-centered cubic structure of SC superalloys, the close-packed plane of atoms is {111} crystal plane. When plastic deformation occurs, dislocations are prone to move along the {111} <110> slip system. The characteristics of fracture formed by the propagation of cracks along the {111} slip plane are inclined planes around 45° , which is octahedral slip mechanism of crack propagation.

Fig.3b shows the fatigue cracks initiated from the surface of the specimen, and the crack initiation area is located on the {111} slip plane. No defect features are observed at the crack initiation area. On the surface of the specimen, in addition to the uniform processing marks, there are also some extrusion morphologies. Fig. 3c shows the extrusion morphology of the surface of the SC superalloys, which is called persistent slip bands (PSBs). Under the action of alternating loads, local slip phenomena occur in the material. As the number of fatigue cycles increases, a large number of irregular slip lines gradually thicken and evolve into regular slip bands. As the number of cycles further increases, slip bands are squeezed out on the surface of the specimen, which is the morphology of PSBs. In Fig. 3c, PSBs are indicated by the white dashed curves, and a large number of PSBs are parallel to each other along the {111} slip planes. Cracks tend to initiate near the PSBs on the surface of the specimen. Fig. 3d shows the morphology of cracks initiating along the PSB. The length of the crack is about 130 μm. By observing the crack morphology in detail, it can be found that the crack propagates along the PSB on the right side, while the crack on the left side is hindered and continues to propagate along other {111} slip planes. The detailed crack propagation path is indicated by the white arrows. From the perspective of fracture mechanics, the type of crack initiation under this condition is composite cracking.

Fig.4 shows the fracture characteristics of low-cycle fatigue under various experimental conditions. The maximum strains are 1.6%, 1.4% and 0.9%, and the number of fatigue cycles of these specimens is greater than 1×10^3. The fracture feature in Fig. 4a only has one extended plane. According to the octahedral slip mechanism, the extended plane is {111} slip plane. Fatigue cracks are initiated near the surface and then propagate along the {111} slip plane until fracture. Fracture surface is flat during the crack propagation stage, while it is rather rough in the instantaneous fracture. Fig. 4b shows the microstructure of the crack initiation area, which displays that the casting pore near the surface is the location of crack initiation. Moreover, the casting pore is located on a small

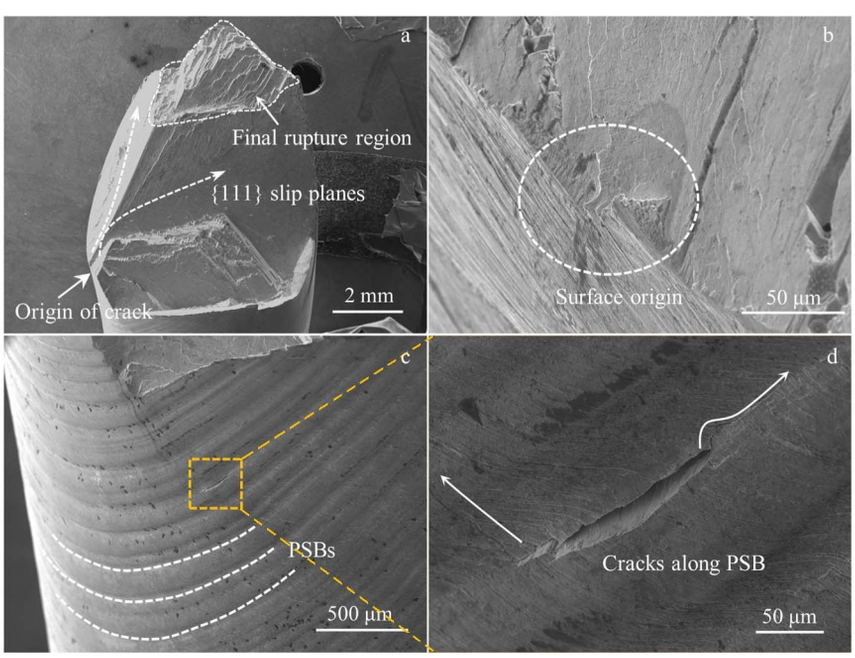

Fig.3 Fracture morphologies and crack initiation characteristics with ε_{max}=2.0%: (a) various stages of crack propagation, (b) crack initiation area, and (c–d) PSBs

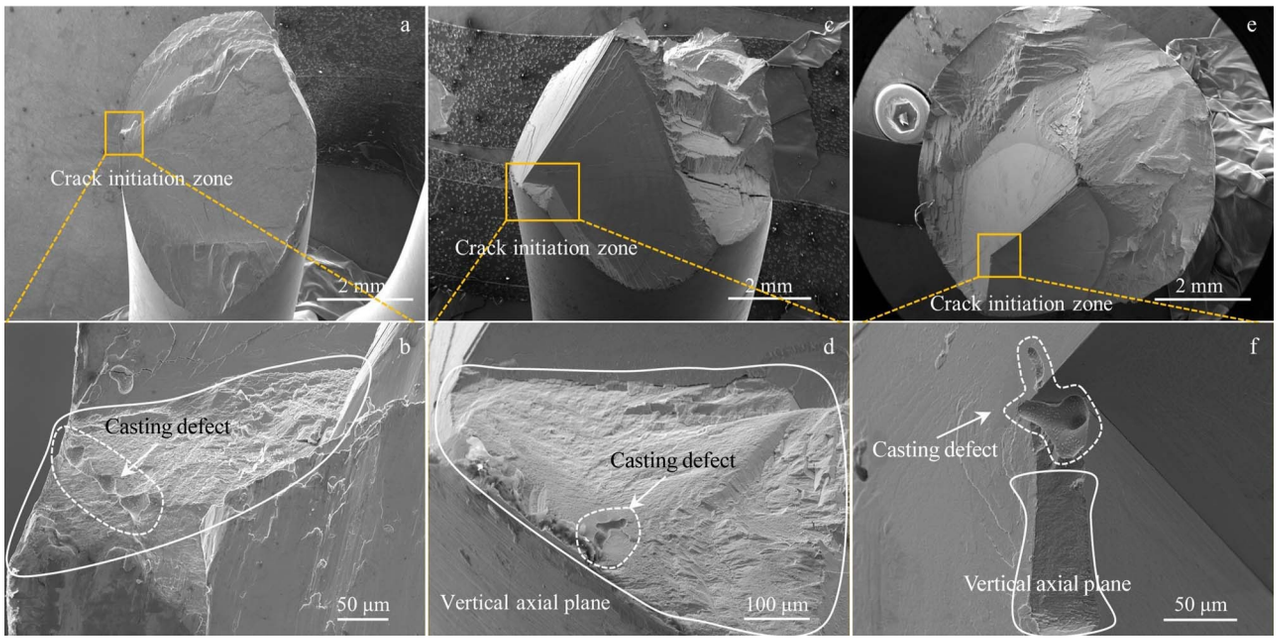

Fig.4 Fracture morphologies and crack initiation characteristics with ε_{max}=1.6% (a–b), ε_{max}=1.4% (c–d), and ε_{max}=0.9% (e–f)

plane perpendicular to the axial force, which is similar to a quadrilateral shape. In addition, another casting pore is located on the {111} slip plane near the small vertical plane, and some secondary cracks appear near the casting pore.

Fig. 4c shows the fracture characteristics with a maximum strain of 1.4% and fatigue cycle of 3563. Fatigue cracks propagate along two different {111} slip planes after crack initiation. In the stage of stable crack propagation, the slip surface exhibits a regular fatigue arc feature, and the instantaneous fracture zone exhibits tearing slip step morphology. As shown in Fig.4c, the crack originates from the casting pore near the surface. Moreover, the casting pore is located on a small plane perpendicular to the axial direction in a triangular shape. After the crack originates from the casting pore, it first fully expands along the triangular plane. When the crack encounters obstacles in the {100} crystal plane, it stably propagates along two different {111} slip planes.

Fig. 4e shows the fracture with a maximum strain of 0.9% and fatigue cycles of 34 294. The number of cycles at the fracture exceeds 1×10^4, which has entered the category of high-cycle fatigue. The location of crack initiation significantly changes due to the increase in fatigue life. As shown in Fig. 4e, fatigue crack originates at the casting pore inside the specimen. The casting pore is located at the intersection of three different {111} slip surfaces. In addition, the surface, where the casting pore is located, is perpendicular to the axial force.

Fig. 5 shows the characteristics of fracture and secondary cracks during the crack initiation stage. The cracks spread around the casting defect and have obvious edges near the defect. Cracks propagate on the small plane with cleavage-like morphology. Fig. 5b shows the microstructure and secondary crack characteristics near casting defects. The microstructure of the matrix consists of γ phase and γ' phase. Between them, the γ' phases present typical cubic morphology. Hence, it can be determined that the crack initiation plane vertical to the axial force is the {100} plane. The mode of cracking initiation along the {100} slip plane belongs to the typical

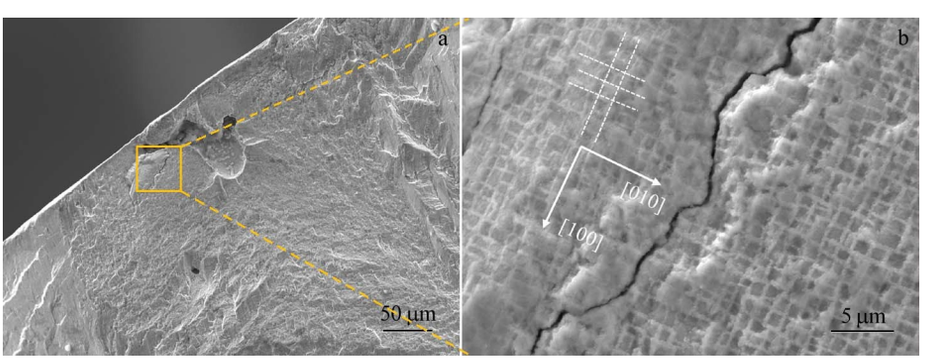

Fig.5 Morphologies of crack initiation and characteristics of secondary cracks with ε_{max}=1.6%: (a) fracture of the initiation area and (b) secondary crack morphology

Mode I cracking.

Fig.6 shows the overall fracture characteristics of the small crack initiation plane. As shown in Fig.6a, the small plane of the triangle contains three stages of crack propagation: crack initiation, stable crack propagation and rapid crack propagation. From Fig.6c, a quasi-circular flat area with a diameter of about 100 μm is firstly formed near the casting defect, and then the crack propagates along the white solid arrows in Fig. 6a towards all sides. Due to the fast propagation rate of cracks on both sides, a structure marked by white dashed curves is formed during the stable propagation stage on the small plane, and the fracture is relatively flat during this stage. In addition, on the small plane, during the rapid propagation stage of cracks, the roughness of the fracture increases and sliding step morphology appears. When the crack fully propagates on the plane perpendicular to the axis, the crack propagation resistance along the {100} slip plane increases. At this time, fatigue crack tends to propagate along the {111} slip plane with low potential. Micro-secondary cracks exist at the intersection of the {100} slip plane and {111} slip plane propagations. As shown in Fig. 6b, the microstructure of γ phase and γ' phase on the {111} slip plane is triangular-like. The cracks mainly propagate along the boundary of γ phase, and some cracks pass through the γ' phase. The crack morphology exhibits Z-shaped propagation characteristic.

2.3 Analysis of plastic deformation during crack initiation

Take the longitudinal section specimens along the fracture surface near the crack initiation area to observe the characteristics. From Fig. 7a, the surface of the fracture is uneven, and the secondary cracks is extended inward on the fracture, with a crack depth of 4–6 μm. In order to obtain the deformation characteristics near the fracture, EBSD was adopted for the longitudinal section analysis near the crack initiation area. Fig.7b shows the band contrast map obtained by EBSD analysis. During the signal acquisition process of the longitudinal section, no crystal plane parameters are collected for the microstructure at a depth of about 5 μm inward from the fracture surface. Analysis shows that the area is under the combined action of tensile and compressive stresses, resulting in distortion of the fracture surface in the crack initiation zone. The incomplete release of surface stress results in the inability to collect crystal plane Kikuchi patterns information in this area.

Fig. 7c shows the inverse pole figure (IPF) map. The longitudinal section along *z*-axis direction shows the {101} crystal plane. No recrystallization features are found on the fracture surface. Fig. 7d shows the Kernel average misorientation (KAM) map near the fracture of the crack initiation area. KAM map is the most commonly used method in the analysis of local misorientation, which is generally used to illustrate the local strain distribution of crystals. According to EBSD data, the map of IPF is actually composed of regular hexagonal pixels, each representing the crystal orientation information contained in the specimen at that position. The local misorientation of each data point can be obtained by averaging the misorientation between each data point and all the data points around a certain radius. KAM plots are obtained after calculating each data point by the analysis software. The strain change of the material is reflected in the change of the local misorientation. The green and yellow-green regions in Fig. 7d indicate locations with notable local misorientation, where the strain changes significantly. No obvious strain distribution is observed in

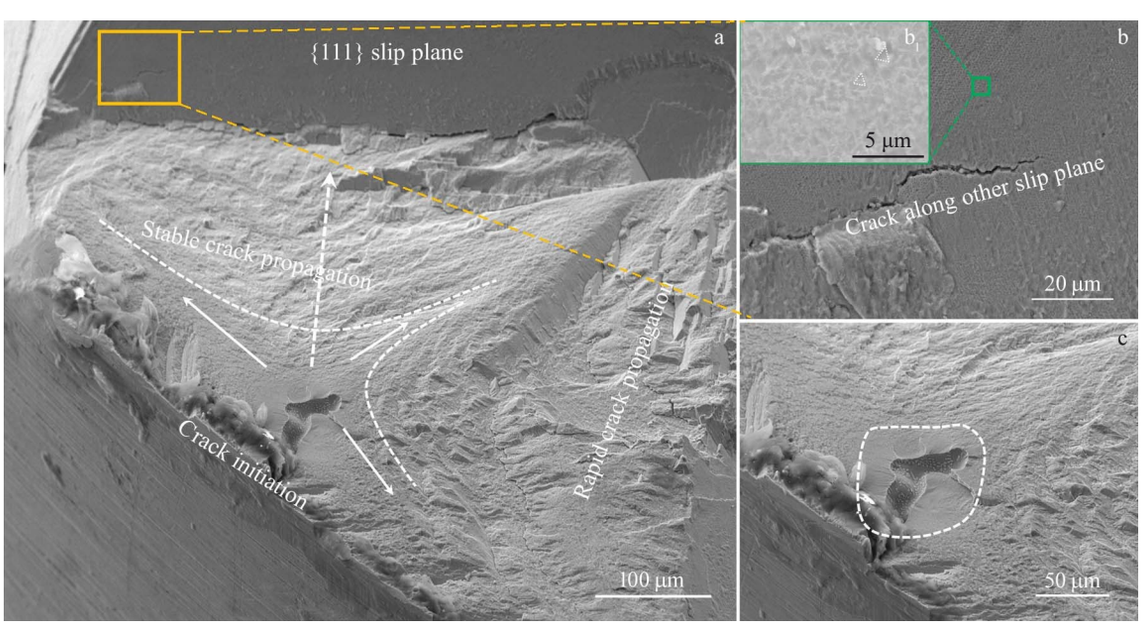

Fig.6 Characteristics of crack initiation and propagation in vertical axial small planes with ε_{max}=1.4%: (a) fracture of the initiation area; (b) fracture characteristic of cracks along other slip plane; (b_1) microscopic morphology of {111} slip plane; (c) casting defect characteristic of crack initiation area

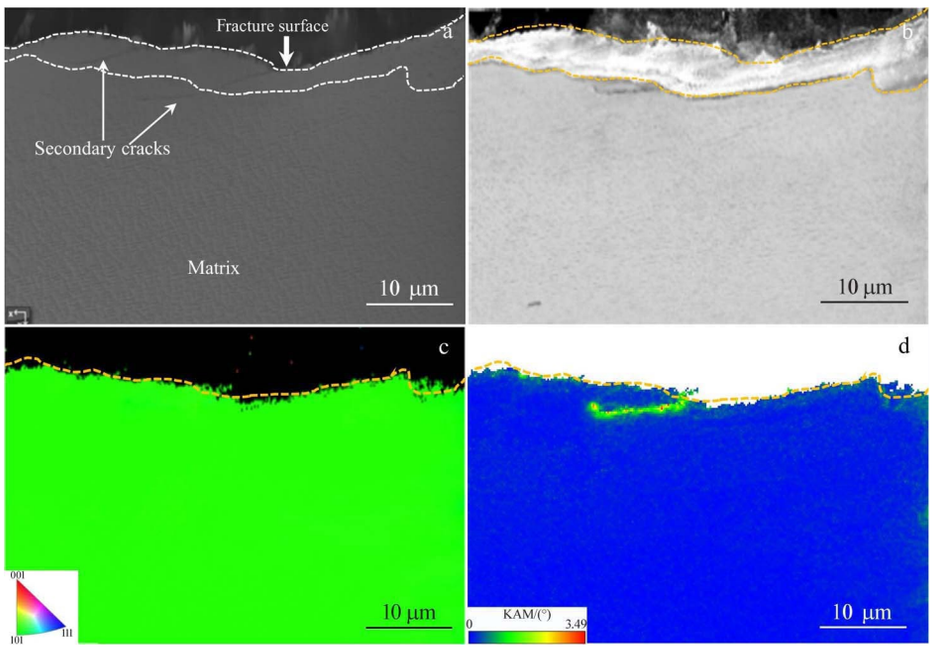

Fig.7 SEM image (a), band contrast map (b), IPF map (c), and KAM map (d) of crack initiation region of specimen with ε_{max}=1.6%

other areas.

2.4 TEM analysis of crack initiation area

In the crack initiation area, FIB technique is used to take a micro-area specimen from the surface of the fracture towards the inside, and the sampling location is shown in Fig. 8a. In order to protect the characteristics of the fracture, platinum was plated on the fracture surface during FIB sampling.

Fig. 8b shows the final specimen morphology after ion-thinning. In TEM analysis, the matrix of γ phase and γ' phase is clearly visible in the longitudinal section. By calibrating the crystal plane index in the [110] crystal direction, it can be inferred from the diffraction pattern that there are superlattice structures in the γ phase and γ' phase. The dislocation density near the surface of the fracture is higher, and gradually

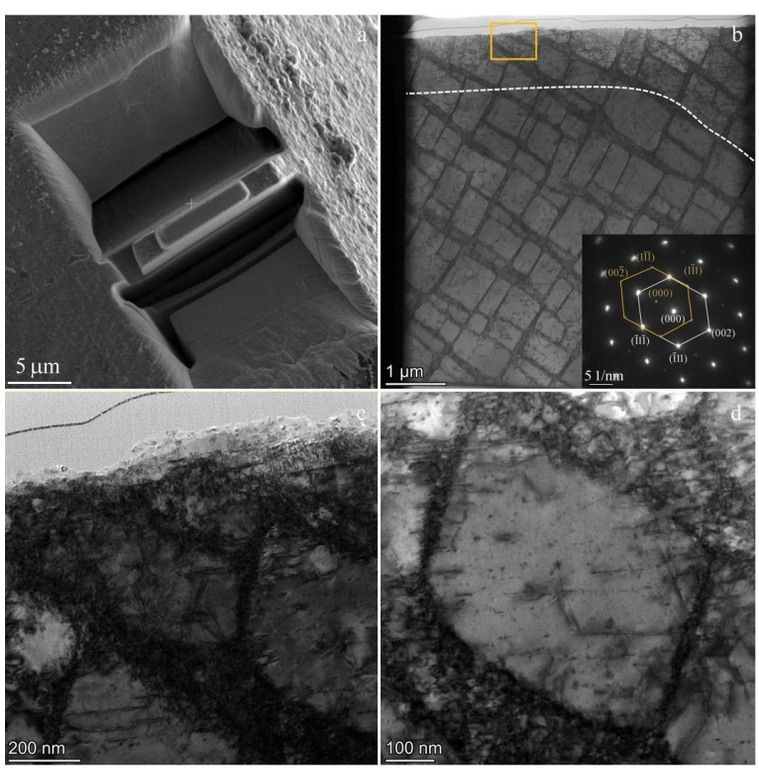

Fig.8 TEM images near the crack initiation area with ε_{max}=1.6%: (a) FIB sampling location; (b) longitudinal section with corresponding SAED pattern; (c) enlarged image of the region marked by the box in Fig.8b; (d) dislocation of the matrix

decreases from the outside to the inside, as shown by the white dashed line. Fig. 8c shows the microstructure near the fracture surface. It can be seen that there is a thin characteristic region on the fracture surface, which is an oxidation region. Below the oxidation zone, dislocations are concentrated in γ phase.

At the same time, a large number of dislocations enter the γ' phase in a climbing manner, causing severe deformation of the γ' phase. Fig. 8d shows the dislocation morphology of the middle of the longitudinal section. At a distance from the fracture surface, a large number of dislocations are concentrated in the γ phase to form a dislocation network, and a few dislocations cut into the boundary of γ' phase. The dislocation density is relatively low in the γ' phase, and the degree of plastic deformation in this region is weak.

Fig. 9 shows the microscopic morphology and element distribution near the fracture surface. The white arrows in Fig.9a indicate the slip line near the fracture, and the slip line is roughly parallel to the fracture surface. There is a slight plastic deformation near the fracture, which makes the original morphology of γ phase and γ' phase disappear. From the EDS mapping of elements, it can be seen that there is an oxide layer of 50–100 nm on the fracture surface. Due to the thin thickness of the oxide layer, it is generally ignored in SEM observation. The oxide layer is marked by a white dashed line. The Ni and Al elements are mainly concentrated in the γ' phase to form the intermetallic compound Ni_3Al, which serves as the strengthening phase of SC superalloys. In

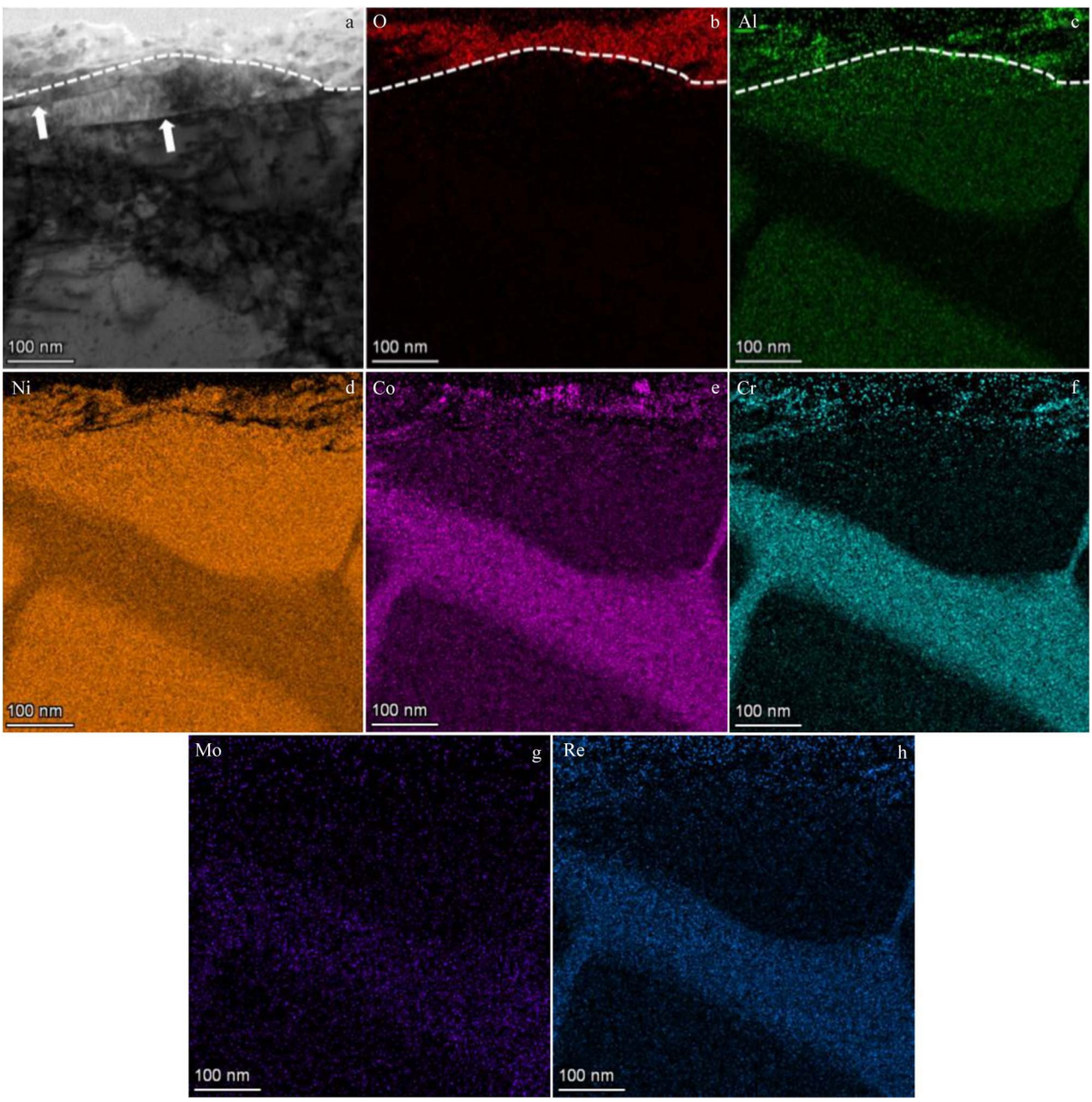

Fig.9 Microstructure (a) and EDS mappings of elements (b–h) in micro-areas near the fracture surface with ε_{max}=1.6%

addition, Co, Cr, Mo, Re and other elements are mainly concentrated in the γ phase as the matrix framework to improve the toughness of SC superalloys.

According to the distribution of elements, the oxide layer on the fracture surface mainly include elements of Ni, Al, Cr and Co, with a higher content of Ni and slightly lower content of Al, Cr and Co elements. This phenomenon is because the fracture surface is fractured along the γ' phase, and the structure of the intermetallic compound Ni_3Al in the γ' phase is disrupted. Meanwhile, the reduction ability of Ni element is greater than that of Al element, so the Ni element is more easily oxidized. The driving force for the segregation of Ni element towards the surface is greater. Therefore, the distribution of Ni element is predominant within the oxide layer. Due to the fact that Cr and Co elements are mainly distributed in the γ phase, the surface segregation path of Cr and Co elements is blocked by γ' phase during the oxidation process. Therefore, the segregation degree of Cr and Co elements in the oxide layer is slightly lower. As the strengthening phase of superalloy, Ni_3Al structure undergoes local segregation of Ni and Al elements due to the influence of temperature and alternating stress, leading to the destruction of the strengthening phase structure and further propagation of cracks during fatigue. No significant element changes are observed near the dislocation and slip lines.

3 Conclusions

1) Under the condition of 530 °C with a strain ratio of 0.05, the number of low-cycle fatigue cycles gradually increases as the maximum strain value decreases. The SC superalloy actually undergoes the cyclic load of tensile and compressive stress during the test. The variation process of actual stress ratio can be divided into two stages at the boundary of 1×10^3 cycles.

2) Under large strain conditions, fatigue cracks are initiated at the PSBs on the surface of the specimen located on the {111} slip plane. No defect features are observed at the crack initiation area. When the maximum strain is below 1.6%, cracks are initiated at the casting defects inside the specimen. The casting defect is located on a small plane perpendicular to the axial force. With the decrease in the maximum strain, the crack initiation position gradually changes from the surface to the sub-surface.

3) The crack initiation zone reveals a slight oxidation of the fatigue fracture surface, with segregation of Ni, Al, Cr and Co elements towards the oxide layer. The presence of stress concentration in the vicinity of the fatigue crack leads to elevated dislocation density on the fracture surface. A large number of dislocations cut into the γ' phase, resulting in the disruption of its reinforced structural integrity and further propagation of the fatigue crack. EBSD results indicate a substantial presence of secondary cracks in the crack initiation zone, accompanied by localized strain behavior near these secondary cracks.

References

1 Arakere N K, Swanson G. *Journal of Engineering for Gas Turbines and Power*[J], 2002, 124(1): 161

2 Hong H U, Kang J G, Choi B G *et al*. *International Journal of Fatigue*[J], 2011, 33(12): 1592

3 Zhou H, Ro Y, Harada H *et al*. *Materials Science and Engineering A*[J], 2004, 381(1–2): 20

4 Vasudevan A K, Sadananda K, Iyyer N *et al*. *International Journal of Fatigue*[J], 2016, 82(2): 120

5 Reed P A S. *Materials Science and Technology*[J], 2013, 25(2): 258

6 Zhang J, Guo Y Y, Zhang M *et al*. *Acta Metallurgica Sinica*[J], 2020, 33(10): 10

7 Zhang L, Zhao L, Jiang R *et al*. *Fatigue & Fracture of Engineering Materials & Structures*[J], 2020(10): 1769

8 Stoltz R E, Pineau A G. *Materials Science and Engineering*[J], 1978, 34(3): 275

9 Hu C Y, Li X L, Liu C K *et al*. *Failure Analysis and Prevention*[J], 2023, 18(1): 8

10 Liu L, Meng J, Liu J L *et al*. *Acta Metallurgica Sinica (English Letters)*[J], 2019, 32(2): 381

11 Povarova K B, Bazyleva O A, Gorbovets M A *et al*. *Russian Metallurgy*[J], 2019, 2019: 687

12 Sundararaman M, Chen W, Wach R P *et al*. *Acta Metallurgica and Materialia*[J], 1992, 40(5): 1023

13 Golubovskiy E R, Svetlov I L, Petrushin N V *et al*. *Russian Metallurgy*[J], 2010, 2010: 941

14 Segersaell M, Leidermark D, Moverare J *et al*. *Materials Science and Engineering A*[J], 2015, 623: 68

15 Liu L, Meng J, Liu J *et al*. *Materials & Design*[J], 2017, 131: 441

16 Li P, Li Q, Jin T *et al*. *International Journal of Fatigue*[J], 2014, 63(1): 137

17 Zhang X, Gao H, Wen Z *et al*. *Advanced Engineering Materials*[J], 2019, 21(2): 647

18 Liu L, Meng J, Liu J L *et al*. *Materials Science and Engineering A*[J], 2018, 734: 1

19 Li L Y, Tian F Z, Li Z *et al*. *Rare Metal Materials and Engineering*[J], 2024, 53(7): 1874

20 Gabb T P, Welsch G, Miner R V *et al*. *Materials Science and Engineering A*[J], 1989, 108(1): 189

21 Brien V, Décamps B. *Materials Science and Engineering A*[J], 2001, 316(1–2): 18

22 Yu J J, Sun X F, Jin T *et al*. *Materials Science and Engineering A*[J], 2010, 527(9): 2379

镍基单晶高温合金的低周疲劳裂纹萌生行为

张金刚[1,2]，刘新灵[1,2]，陈　星[1,2]，李　振[1,2]，李乐宇[1,2]，刘昌奎[1,2]
(1. 中国航发北京航空材料研究院 中国航发失效分析中心，北京 100095)
(2. 航空材料检测与评价北京市重点实验室，北京 100095)

摘　要：对镍基单晶高温合金在530 ℃的低周疲劳裂纹萌生行为进行研究。结果表明：在530 ℃、应变比0.05时，疲劳裂纹的萌生行为与最大应变的变化关系密切。在最大应变为2.0%时，疲劳裂纹在试样表面的驻留滑移带位置萌生，且萌生平面位于｛111｝滑移面，萌生位置未见缺陷。当最大应变低于1.6%时，裂纹萌生于试样亚表面或内部的铸造疏松位置，且铸造疏松位于垂直轴向力的｛100｝滑移面。裂纹沿｛100｝滑移面萌生后经小阶段扩展后再沿不同｛111｝滑移面进行扩展。随最大应变减小，裂纹萌生位置逐渐由表面向内部转变。裂纹萌生区存在沿断口表面向内部延伸的二次裂纹，且二次裂纹附近存在明显应力集中。在裂纹萌生区的断口表面附近位错密度较高，大量位错切入γ'相。断口表面存在50~100 nm的氧化层，Ni、Al、Cr和Co元素存在向表面氧化层的偏析行为。

关键词：裂纹萌生；低周疲劳；单晶高温合金；铸造疏松；位错

作者简介：张金刚，男，1995年生，博士，中国航发北京航空材料研究院中国航发失效分析中心，北京 100095，E-mail：jingangpri@163.com